Cloud-Top Motion Variation of a Landfall Typhoon Observed by Geostationary Satellite Imagery

Gang Zheng, *Senior Member, IEEE*, Jianguo Liu, *Senior Member, IEEE*, Liang Wu, Peng Chen, Qiaoyan Wu, Jie Ming, and Lizhang Zhou, *Member, IEEE*

***Abstract*—Typhoons' rapid variation makes effective hazard prevention difficult, which remains a challenging research topic requiring novel observation technology and analysis methodology. We developed an automatic methodology for mining the information on the rapid variation of typhoon cloud-top motion from high-spatial-temporal-resolution satellite cloud images, which has steps of estimating and decomposing the typhoon cloud-top motion, locating the typhoon cloud-top center, and analyzing the motion and center position variations. The Gaofen-4 satellite acquired 50-m-1-min-resolution cloud images of Typhoon Megi's (2016) landfall over mountainous Taiwan Island. The data provide an excellent chance to explore what such high-spatial-temporal-resolution successive observations can tell about the cloud-top motion variation of a typhoon landfall using the methodology. Before its landfall, Typhoon Megi's cloud-top center dramatically increased the northwestward migration speed from ∼22 to ∼58 km/h in only ∼2.5 h. It also presented small-scale oscillation along its migration path with a 1.6-to-2.4-km amplitude, a 31-to-33-km spatial period, and a 1.46-to-1.48-h temporal period. We averaged the motion speeds (velocity magnitudes) in each motion field to assess the field strength. The so-calculated cloud-top average rotation speed of Typhoon Megi decreased quickly during landfall. Meanwhile, its average divergence speed increased dramatically by ∼30% in a short period of ∼2.5 h, reaching ∼2 times the rotation speed. This result means that Megi's cloud-top motion rapidly changed from a typical rotation motion-dominated status to a divergence motion-dominated status. This rapid transformation from typical rotation motion dominance to divergence motion dominance implies intense upward warm and moist airflows that cause severe precipitation.**

***Index Terms*—Atmospheric motion vectors (AMVs), field decomposition, geostationary satellite, motion field, tropical cyclone (TC), typhoon.**

Manuscript received 25 October 2023; revised 12 January 2024 and 23 February 2024; accepted 13 March 2024. Date of publication 18 March 2024; date of current version 8 April 2024. This work was supported in part by the National Natural Science Foundation of China under Grant 42306216, in part by Zhejiang Provincial Natural Science Foundation of China under Grant LR21D060002, in part by the Key R&D Project of Shandong Province under Grant 2019JZZY010102, in part by the Innovation Group Project of Southern Marine Science and Engineering Guangdong Laboratory (Zhuhai) under Grant 311021004, in part by the Chinese Academy of Sciences Program under Grant Y9KY04101L, in part by the National Natural Science Foundation of China Grant 42175050, and in part by the Youth Innovation Promotion Association CAS Y2021030. *(Corresponding authors: Gang Zheng; Peng Chen.)*

Gang Zheng is with the State Key Laboratory of Satellite Ocean Environment Dynamics, Second Institute of Oceanography, Ministry of Natural Resources, Hangzhou 310012, China, also with Ocean College, Zhejiang University, Zhoushan 316021, China, also with the College of Oceanography, Hohai University, Nanjing 210098, China, and also with Southern Marine Science and Engineering Guangdong Laboratory (Zhuhai), Zhuhai 519082, China (e-mail: zhenggang@sio.org.cn).

Jianguo Liu is with the Department of Earth Science and Engineering, Imperial College London, SW7 2AZ London, U.K., and also with the State Key Laboratory of Satellite Ocean Environment Dynamics, Second Institute of Oceanography, Ministry of Natural Resources, Hangzhou 310012, China.

Liang Wu is with the Center for Monsoon System Research, Institute of Atmospheric Physics, Chinese Academy of Sciences, Beijing 100029, China.

Peng Chen is with the State Key Laboratory of Satellite Ocean Environment Dynamics, Second Institute of Oceanography, Ministry of Natural Resources, Hangzhou 310012, China (e-mail: chenpeng@sio.org.cn).

Qiaoyan Wu is with the State Key Laboratory of Satellite Ocean Environment Dynamics, Second Institute of Oceanography, Ministry of Natural Resources, Hangzhou 310012, China, and also with the School of Oceanography, Shanghai Jiao Tong University, Shanghai 200030, China.

Jie Ming is with the School of Atmospheric Sciences, Nanjing University, Nanjing 210023, China.

Lizhang Zhou is with the State Key Laboratory of Satellite Ocean Environment Dynamics, Second Institute of Oceanography, Ministry of Natural Resources, Hangzhou 310012, China.

Digital Object Identifier 10.1109/JSTARS.2024.3378572

I. Introduction

TROPICAL cyclones (TCs) are severe weather systems striking global coast regions with extreme winds and precipitations. Future projections based on data from recent history consistently suggest an increase in the mean intensity of global TCs over the coming decades [1], [2], [3], [4]. Intensification of TC activities is expected to increase the population exposed to TCs every year significantly, exacerbating disaster risk and causing enormous environmental damage and economic loss [5], [6].

Hazards usually occur during TC landfalls [7], [8]. Studying TC landfalls is particularly important in the western North Pacific, where the TC frequency is high, accounting for >30% of the global TCs [8], [9], [10]; TCs are usually called typhoons in this region. When interacting with complicated topography, landfalls often induce rapid changes in typhoon systems, such as high-frequency variations in typhoons' migrations, airflows, and precipitations. The rapid variation of typhoons makes accurate forecasts difficult and thus hinders effective hazard prevention, especially for remote areas lacking ground-based radars.

With the development of remote sensing technology, TC observation data is of greater diversity and quantity than ever before. Spaceborne microwave scatterometers [11], [12], [13] and radiometers [14] provide global sea surface wind measurements even beneath heavy clouds of TCs. In addition, spaceborne synthetic aperture radars have been widely used to capture finer structures of TCs at the sea surface because of much higher spatial resolution [15], [16], [17], [18], [19], [20], [21]. However, observing TC motion variation over coast zones and inland regions depends mainly on ground-based radars. Although spaceborne remote sensing technology has the advantage of global coverage over ground-based radars and

aircraft reconnaissance, the polar-orbiting microwave sensors have shortcomings of inadequate spatial-temporal resolution while high spatial resolution and imaging rate are essential to capture typhoons' high-frequency variation occurring in a short time. Therefore, novel observation technology and analysis methodology need to be explored to provide new perspectives.

Some indices can be derived from a single satellite cloud image to depict a TC system's status using techniques such as the original Dvorak and its modified versions commonly used to generate the 3- or 6-h-interval best track (BT) data sets. A different way, as we did, is to directly estimate cloud motion vectors by tracking cloud features in successive images. These cloud motion vectors are called atmospheric motion vectors (AMVs), representing the horizontal components of the winds at the cloud level. However, TC clouds are typically of fast-evolving due to deformation, evaporation, and vertical shear. Some TC cloud features are too short-lived to be tracked by routine imaging intervals of meteorological satellites ($\geq$10 min) [22].

Gaofen-4 (GF-4) is a Chinese high-resolution geostationary satellite with spatial resolutions and imaging rates up to 50 m and 20 s, respectively. The comparison study between the GF-4 satellite and the Himawari-8 satellite suggests that higher spatial-temporal resolution can capture the fast cloud-shape changes and fine dynamical features of typhoons, especially in their central areas, and thus enable the typhoon AMV derivation and AMV-based typhoon center locating [22]. The GF-4 satellite acquired 50-m-1-min-resolution cloud images that captured Typhoon Megi (2016) landfall event over Taiwan Island, where the giant Central Mountain Range characterizes the landscape. The Central Mountain Range is north-northeast to south-southwest oriented, $\sim$300 km long, and $\sim$80 km wide with an average elevation of $\sim$3000 m, and there are 22 peaks higher than 3500 m. Because of the size and high relief of the mountain range, the GF-4 images of Typhoon Megi provide us with an excellent data source to investigate what such a high-spatial-temporal-resolution successive observations of typhoon top clouds can tell about the cloud-top motion variation during typhoon landfall.

We give a fully automatic analysis methodology in this article for mining the information of the rapid variation of typhoon cloud-top motion from the GF-4 images. The methodology comprises the methods developed in our previous studies [23], [24] to estimate the typhoon cloud-top motion and derive the typhoon cloud-top rotation and divergence motion fields and center positions. It also includes the methods proposed in this article to extract migration oscillation kinematic characteristics of the typhoon cloud-top center.

The rest of this article is organized as follows. Section II describes the data of the GF-4 and other satellites used in the study. Section III introduces our automatic analysis methodology of processing GF-4 images and extracting the kinematic characteristics of the migration oscillation of Typhoon Megi's cloud-top center. Section IV presents the results. Section V is a summary.

II. Satellite Data

A. GF-4 Satellite Data

The GF-4 satellite has a Complementary Metal Oxide Semiconductor array sensor. The sensor has five visible-near infrared (VNIR) spectral bands (0.45–0.90, 0.45–0.52, 0.52–0.60, 0.63–0.69, and 0.76–0.90 μm) and can image the Earth at a 50-m resolution [24]. The acquired images have 10 240 $\times$ 10 240 pixels, covering about 512 km $\times$ 512 km.

Typhoon Megi landed over Hualien of Taiwan Island at $\sim$06:00, 27 September 2016 (UTC). Typhoon Megi was captured in a series of images at 1-min intervals by GF-4 during its landfall event in two imaging sessions of 02:00–03:53 and 05:00–06:53 UTC. The sensor's first band is a panchromatic band (0.45–0.90 μm) covering the whole VNIR spectral range and thus has a higher signal-to-noise ratio than the other bands. Therefore, the GF-4 first-band images of the two imaging sessions were collected to derive pixel-wise AMVs at 1-min intervals.

B. Other Satellite Data

The CloudSat polar-orbiting satellite, equipped with a 94-GHz nadir-looking cloud profiling radar, measures radar reflectivity at different altitudes along its tracks and classifies clouds [25], [26], [27]. The CloudSat satellite flew over the west of Typhoon Megi's central area at 05:26 UTC. This extra information enables us to check the vertical distributions of radar reflectivity and cloud type of Typhoon Megi along the CloudSat satellite's track. Moreover, the upper boundary of the high radar reflectivity region suggests the GF-4 satellite-observed clouds and derived AMVs would be mainly at $\sim$14 to 17.5 km altitude.

The tropical rainfall measuring mission (TRMM) multisatellite precipitation analysis (TMPA) 3B42 version-7 products are gridded data available every 3 h with a grid size of 0.25° $\times$ 0.25°. The 3B42 algorithm generates the products by first blending the remotely-sensed microwave measurements (of the TRMM microwave imager, the special sensor microwave/imager, the advanced microwave scanning radiometer, and the advanced microwave sounding unit) and then filling the gaps with the microwave-calibrated infrared estimates [28]. We used the TMPA products to show the precipitation variation of Typhoon Megi.

III. Methodology

A. Processing GF-4 Images

The whole image processing procedure has five steps as illustrated in Fig. 1.

1) Select GF-4 images matching the typhoon landfall event to obtain the working image sequences and group every two consecutive images with a 1-min interval as a pair.
2) Derive pixel-wise disparity maps from the image pairs, and generate the cloud-top motion field by dividing the disparities in the maps by the time interval.
3) Decompose the cloud-top motion field into the rotation, divergence, and harmonic motion fields.
4) Automatically locate typhoon cloud-top center positions from the cloud-top rotation motion field.
5) Calculate the average values of the motion speeds (magnitudes of velocity vectors) in the cloud-top rotation and divergence motion fields within the circles centered at the typhoon cloud-top center positions.

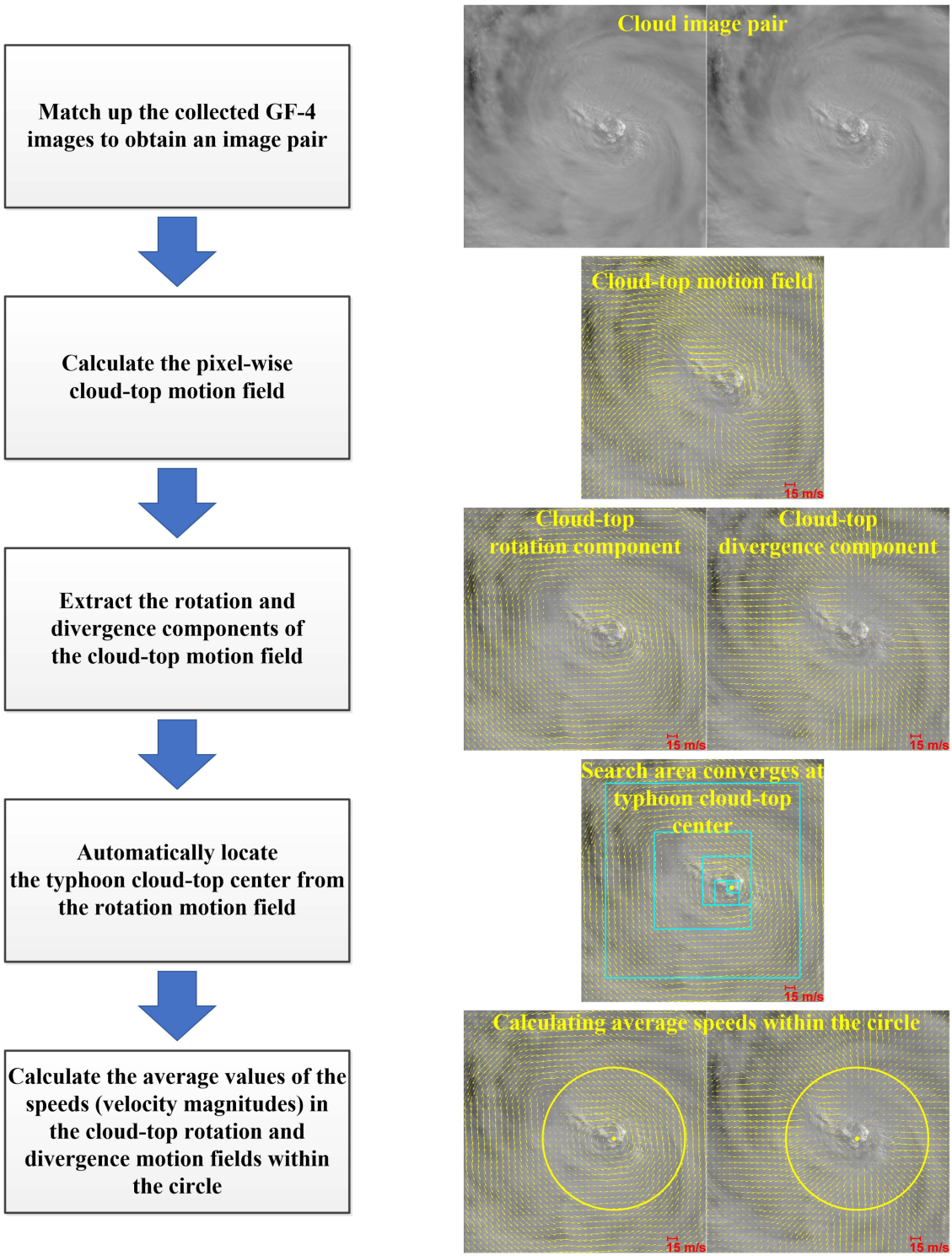

Fig. 1. Flowchart of processing GF-4 images. A pair of GF-4 images are collected. The cloud-top motion field is derived from the pair. The rotation and divergence components are extracted from the cloud-top motion field. The typhoon cloud-top center is automatically located as the search area (cyan boxes) converges. The speeds (magnitudes of velocity vectors) of the cloud-top rotation and divergence motion fields are spatially averaged within a circle (yellow) centered at the typhoon cloud-top center (yellow dot).

The thick clouds of a typhoon are typically opaque to VNIR sensors and rich in texture. It is therefore possible to use the phase correlation (PC) algorithm to estimate the translation between every pair of corresponding pixels in a cloud image pair by comparing the pixels' neighborhood image patches [23]. The principle of the PC algorithm is the well-known Fourier shift property. A linear translation between two resembling image patches in the spatial domain results in a phase shift in the

frequency domain of their Fourier Transforms [23], [29], [30], [31]. The translation between two overlapped image patches can then be identified directly in the frequency domain at subpixel magnitude through the areal correlation between them, based on the spatial textures formulated by all the patch pixels involved in the comparison. The above-mentioned patch-matching process can proceed with pixel-by-pixel scanning to derive pixel-wise disparity maps in image line and column directions.

We grouped GF-4 images of Typhoon Megi in a time sequence in consecutive 1-min-interval pairs. Then, the pixel-wise disparity maps of these pairs were generated using the phase correlation image analysis system, which integrates the PC algorithm [29], [30]. The pixel-wise cloud-top motion field was produced by dividing the disparities by the time interval. Each motion vector in the field is an AMV.

The successive images-derived typhoon cloud-top motion field could include artificial translation besides the typhoon's rotation, divergence, and migration. The artificial translation is largely the scene shift resulting from the camera steering to chase the typhoon system or the imaging platform's minor instability. The translation due to platform instability will become relatively more significant when the time interval between the two images is getting smaller because the translation of camera steering increases proportionally with time. In other words, the camera steering-induced translation is greater in a longer time interval and smaller in a shorter time interval. In contrast, the platform instability-induced translation is random and thus not proportional to the imaging time interval. All the above-mentioned artificial translation mingles with the typhoon's motion. To our knowledge, existing remote sensing image analysis methods using images of much lower spatial-temporal resolution have not considered this artificial translational motion.

Recently, we developed a Green function-based vector field decomposition algorithm [24] for decomposing a motion field into the rotation, divergence, and harmonic components within a limited domain with an open boundary as follows.

A two-dimensional (2-D) motion field $\vec{V}$ inside a domain Ω can be decomposed as

$$\vec{V} = \vec{V}_\psi + \vec{V}_\chi + \vec{V}_0 \tag{1}$$

where $\vec{V}_\psi$ has the same curl as $\vec{V}$ and is divergence-free, and $\vec{V}_\chi$ has the same divergence as $\vec{V}$ and is curl-free. Thus, the residual field (harmonic field) $\vec{V}_0$ is free of both curl and divergence. The decomposition based on the above-mentioned definition is not unique, but a unique decomposition can be resolved with a physical constraint appropriately relevant to the problem. The cloud-top motion field ($\vec{V}$) should be decomposed with such a physical constraint: within a limited domain Ω with an open boundary, which means there is no real physical interface between the limited domain and its surrounding free space. Under this physical constraint, the rotation and divergence motion fields ($\vec{V}_\psi$ and $\vec{V}_\chi$) can be written as [24]

$$\vec{V}_\psi(r) = \frac{1}{2\pi}\text{P.V.}\iint_\Omega \overrightarrow{z} \times \frac{\vec{r}-\vec{r}'}{|\vec{r}-\vec{r}'|^2}\overrightarrow{z} \cdot \nabla \times \vec{V} d\Omega' \tag{2}$$

$$\vec{V}_\chi(r) = \frac{1}{2\pi}\text{P.V.}\iint_\Omega \frac{\vec{r}-\vec{r}'}{|\vec{r}-\vec{r}'|^2}\nabla \cdot \vec{V} d\Omega' \tag{3}$$

where P.V. denotes Cauchy principal value. $\overrightarrow{z}$ is the unit vector normal to the plane of Ω. $\frac{1}{2\pi}\overrightarrow{z} \times \frac{\vec{r}-\vec{r}'}{|\vec{r}-\vec{r}'|^2}$ and $\frac{1}{2\pi}\frac{\vec{r}-\vec{r}'}{|\vec{r}-\vec{r}'|^2}$ are the cloud-top rotation and divergence motion fields in free space derived from the rotation and divergence point sources at the position $\vec{r}'$. The computation of (2) and (3) can be simplified to two 2-D convolution operations and can be efficiently carried out by fast Fourier and inverse Fourier transforms [24].

We used the algorithm to remove the harmonic component (that includes the artificial translation) while extracting the cloud-top concentric (rotation and divergence) motion fields of Typhoon Megi under the physical constraint.

Rotation is one of the essential characteristics of a typhoon. Therefore, the typhoon cloud-top center can be located from the cloud-top rotation motion field.

Our automatic center location algorithm [24] is based on a simple motion direction-based index embedded in an efficient pyramid search scheme. The located center is the point at which motion directions converge. The algorithm is briefly introduced below.

Motion directions converging at the typhoon cloud-top center is typical for a typhoon's cloud-top rotation motion field. Thus, we designed a motion direction-based index to search the center of concentric motion in the motion field. For a perfectly symmetric rotation motion field, the direction vector (a normalized motion vector with a magnitude of one) at any location within the neighborhood of the motion center has its opposite counterpart at the symmetric location. Thus, the magnitude of the mean of the direction vectors should equal zero. The greater the magnitude is, the less concentric the motion. Therefore, we can use this magnitude as an index to search the center of the typhoon's cloud-top rotation motion field. We embedded the index in an efficient pyramid-searching scheme with an iteration procedure [24]. In each iteration step, the index values of several candidate areas are calculated, which are the magnitudes of the means of the direction vectors within each of the candidate areas. The candidate area with the minimum index value is selected as the further search area and partitioned into several smaller candidate areas for the next iteration step. With the iteration step increasing, the search area will converge at the concentric motion center. For example, the cyan boxes in Fig. 1 show the pyramid searching procedure where the search area converges at the typhoon cloud-top center (the yellow dot).

The algorithm was used to locate the cloud-top center of Typhoon Megi at 1-min intervals to investigate the center migration.

We further calculated the average values of the motion speeds (magnitudes of velocity vectors) in the cloud-top rotation and divergence motion fields, respectively, within the circles centered at the cloud-top center positions of Typhoon Megi. These speed data are indicative of the strengths of the cloud-top rotation and divergence motion fields and are essential to the investigation of the rapid field-strength variation. The radius of the circles was set to 150 km to ensure that the circles were within the GF-4 images.

B. Extracting Typhoon Migration Oscillation Kinematic Characteristics

As seen in Section IV-A, the 50-m-1-min-resolution center locating reveals the cloud-top center of Typhoon Megi had small-scale oscillation along its northwestward migration path. To quantitatively analyze the oscillation characteristics (e.g., oscillation amplitude, spatial period, temporal period, etc.), two methods are proposed: one is based on sine-curve fitting and the other is precession-model-curve fitting.

Taking the transformation of coordinate system rotation and translation, we can establish a five-parameter (A, k, θ, x_0, and y_0) model (4) to represent a sine curve along any direction with any amplitude, spatial angle frequency, and initial phase

$$\begin{aligned} &A \cdot \sin\left(k \cdot \left((x+x_0)\cdot\cos\theta + (y+y_0)\cdot\sin\theta\right)\right) \\ &\quad +(x+x_0)\cdot\sin\theta - (y+y_0)\cdot\cos\theta \end{aligned} = 0 \tag{4}$$

where (x, y) is the coordinate of a position on the sine curve. The parameters A and k are oscillation amplitude and spatial angle frequency of the sine curve. θ, x_0, and y_0 determine the axis along which the sine curve oscillates.

Equation (4) fits a given sequence of position samples denoted as $(x_1, y_1), \ldots, (x_i, y_i), \ldots, (x_I, y_I)$. The five parameters of (4) can be determined by minimizing the square sum of the residuals (SSRs) of the position samples on the left side of (4) as

$$\begin{aligned} &\left(\widehat{A}, \widehat{k}, \widehat{\theta}, \widehat{x_0}, \widehat{y_0}\right) \\ &= \underset{A,k,\theta,x_0,y_0}{\arg\min} \sum_{i=1}^{I} \\ &\quad \times \left(\begin{array}{c} A \cdot \sin\left(k \cdot \left((x_i+x_0)\cdot\cos\theta + (y_i+y_0)\cdot\sin\theta\right)\right) \\ +(x_i+x_0)\cdot\sin\theta - (y_i+y_0)\cdot\cos\theta \end{array}\right)^2 \end{aligned} \tag{5}$$

where $\widehat{A}$, $\widehat{k}$, $\widehat{\theta}$, $\widehat{x_0}$, and $\widehat{y_0}$ denote the determined parameters of the best-fit sine curve. The genetic algorithm can solve the nonlinear multivariable optimization problem of (5). It is a global optimization technique based on genetics and natural selection principles, imitating the evolution of living beings. In the genetic algorithm's optimization procedure, sets of candidate values of the parameters are encoded as sequences of numbers (called genes). The genes go through crossover, mutation, and selection (selecting the genes with smaller SSRs to be preserved) to generate new genes. After generations of genes, the candidate values corresponding to the gene with the smallest SSR are considered the optimized values of the parameters.

With the five parameters determined, the spatial period (denoted by $\widehat{\lambda}$) of the best-fit sine curve is

$$\widehat{\lambda} = 2\pi \Big/ \left|\widehat{k}\right| \tag{6}$$

and the oscillation phase (denoted by $\widehat{\varphi}$) of a position (x, y) on the best-fit sine curve is

$$\widehat{\varphi} = \frac{(x+x_0)\cdot\cos\widehat{\theta} + (y+y_0)\cdot\sin\widehat{\theta}}{\widehat{\lambda}}. \tag{7}$$

Then, the number (denoted by $\widehat{N}_{cycles}$) of the oscillation cycles occupied by the sequence of position samples can be estimated as

$$\widehat{N}_{cycles} = \left|\widehat{\varphi}_I - \widehat{\varphi}_1\right| \Big/ 2\pi \tag{8}$$

where $\widehat{\varphi}_1$ and $\widehat{\varphi}_I$ are the estimated oscillation phases of the first position sample (x_1, y_1) and the last sample (x_I, y_I) in the sequence.

In this study, (4) fits the sequence of the cloud-top center positions of Typhoon Megi during the oscillation. $\widehat{\theta}$, $\widehat{x_0}$, and $\widehat{y_0}$ represent the estimated axis of Typhoon Megi's migration along which its cloud-top center oscillates. $\widehat{A}$ and $\widehat{\lambda}$ are the estimated amplitude and spatial period of the oscillation. The temporal period of the oscillation can be estimated by dividing the sequence's time length (T_{seq}) by the number ($\widehat{N}_{cycles}$) of the oscillation cycles of the sequence

$$\widehat{T} = T_{seq} \Big/ \widehat{N}_{cycles}. \tag{9}$$

The migration speed of Typhoon Megi's cloud-top center along the axis is

$$\widehat{u} = \widehat{\lambda} \Big/ \widehat{T}. \tag{10}$$

For the precession model-based method, the self-rotation axis of a typhoon is presumed to rotate around the vertical axis during its migration. Thus, a typhoon cloud-top center's motion can be considered a superposition of a precession and a migration. Then, a six-parameter (A, ω, u_x, u_y, x_0, and y_0) model can formulate the typhoon cloud-top center's position (x, y) at the time t

$$\begin{cases} x(t) = A\cdot\cos(\omega t) + (u_x t + x_0) \\ y(t) = A\cdot\sin(\omega t) + (u_y t + y_0) \end{cases}. \tag{11}$$

The first and second parts on the right side of (11) represent the precession and migration, respectively. A and ω are the amplitude and angular frequency of the precession, respectively. u_x and u_y are two components of the migration velocity, and thus u_x, u_y, x_0, and y_0 determine the migration axis along which the typhoon cloud-top center oscillates.

The six parameters of (11) can be determined based on a given sequence of the position samples $(x_1, y_1), \ldots, (x_i, y_i), \ldots, (x_I, y_I)$ at the times of $t_1, \ldots, t_i, \ldots, t_I$

$$\begin{aligned} &\left(\widehat{A}, \widehat{\omega}, \widehat{u_x}, \widehat{u_y}, \widehat{x_0}, \widehat{y_0}\right) \\ &= \underset{A,\omega,u_x,u_y,x_0,y_0}{\arg\min} \sum_{i=1}^{I} \left((x_i - x(t_i))^2 + (y_i - y(t_i))^2\right). \end{aligned} \tag{12}$$

The above can be solved using the genetic algorithm.

The sign of $\widehat{\omega}$ determines the estimated rotation direction of the typhoon cloud-top center (positive sign for anticlockwise and negative sign for clockwise). $\widehat{u_x}$, $\widehat{u_y}$, $\widehat{x_0}$, and $\widehat{y_0}$ determine the estimated axis of the migration. The migration speed of the typhoon cloud-top center along the axis is

$$\widehat{u} = \sqrt{\widehat{u_x}^2 + \widehat{u_y}^2}. \tag{13}$$

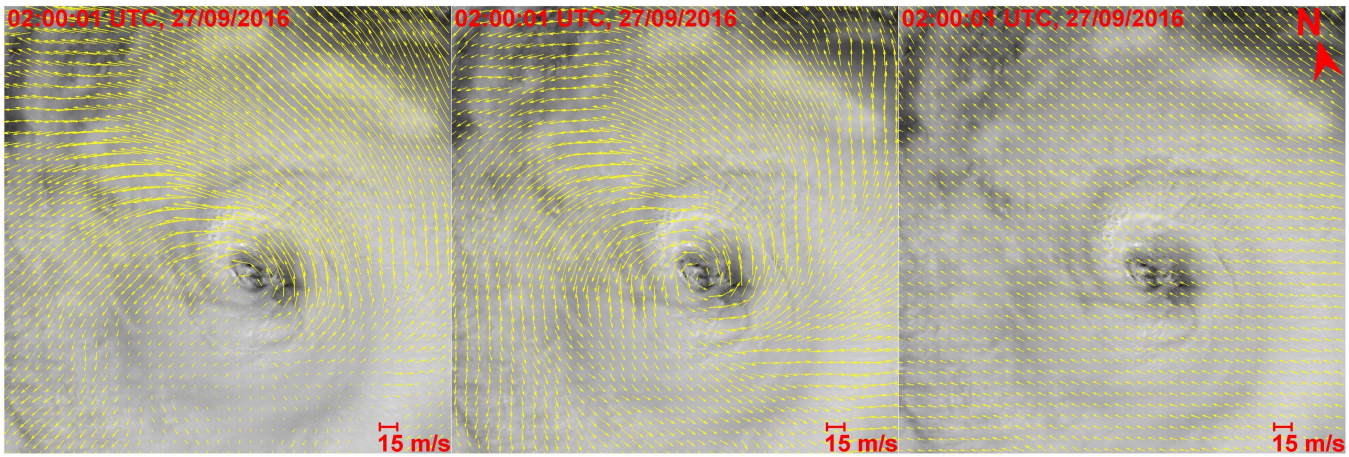

Fig. 2. GF-4 images-derived cloud-top motion field (a) before and (b) after removing the harmonic component (c). Backgrounds are cloud images acquired by the GF-4 satellite.

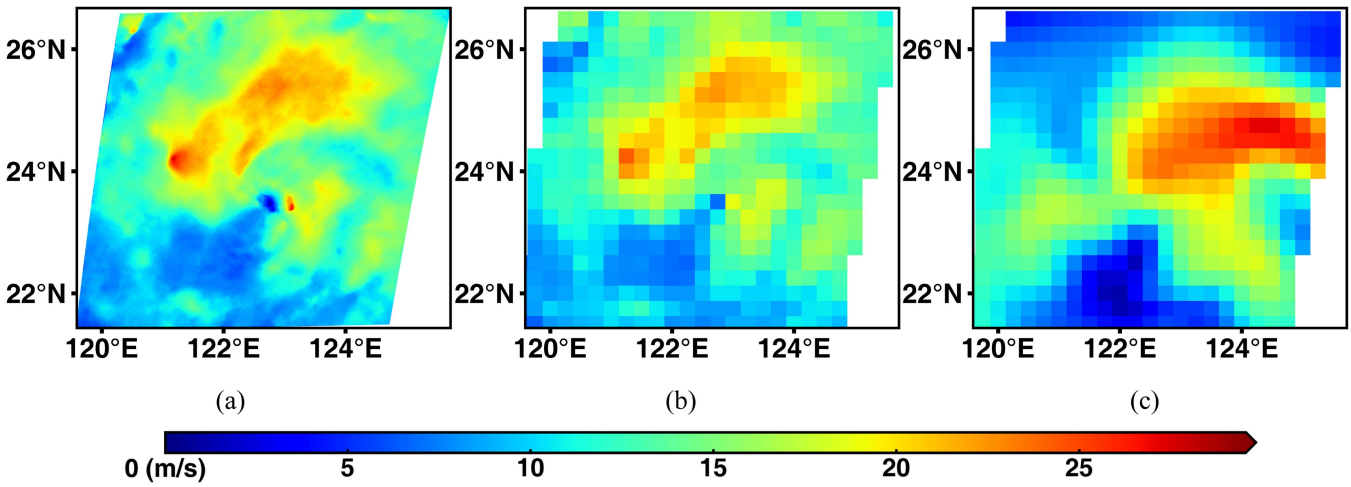

Fig. 3. (a) GF-4 images-derived cloud-top motion speed data after removing the harmonic component, (b) its subsampled result, and (c) the ERA5 horizontal wind speed data at 100-hPa level after removing the harmonic component.

The temporal and spatial periods of the precession are

$$\widehat{T} = 2\pi/|\widehat{\omega}| \tag{14}$$

and

$$\widehat{\lambda} = \widehat{u} \cdot \widehat{T}. \tag{15}$$

IV. Results

We processed the GF-4 images following the procedure in Section III-A and presented the results in this section.

Fig. 2(a) shows Typhoon Megi's cloud-top motion field derived from the GF-4 images at 02:00 UTC. The field pattern is inconsistent with the cloud features, as the field rotation center and the cloud rotation center are misaligned. If we used these cloud-top motion data directly, we could fail to locate the true typhoon cloud-top center and then implement the further analysis correctly. However, after removing the harmonic component [see Fig. 2(c)], the cloud-top motion field comprises Typhoon Megi's concentric (rotation and divergence) motions only and thus becomes much more consistent with the cloud features [see Fig. 2(b)].

Fig. 3(a) presents the GF-4 images-derived cloud-top motion speeds at 02:00 UTC with the harmonic component removed. The data in Fig. 3(a) are subsampled, using the arithmetic mean method, into 0.25° grids of the European Centre for Medium-Range Weather Forecasts (ECMWF) Reanalysis v5 (ERA5) as shown in Fig. 3(b). Fig. 3(c) presents the ERA5 horizontal wind speeds at 100-hPa level (about 16-km altitude comparable to Typhoon Megi's overall cloud-top altitude suggested by the CloudSat satellite), with the harmonic component removed. We can see that the subsampled speed data in Fig. 3(b) and the ERA5 speed data in Fig. 3(c) are consistent in the overall pattern.

The upper panel of Fig. 4 shows that the located positions (magenta dots) of Typhoon Megi's cloud-top center form two

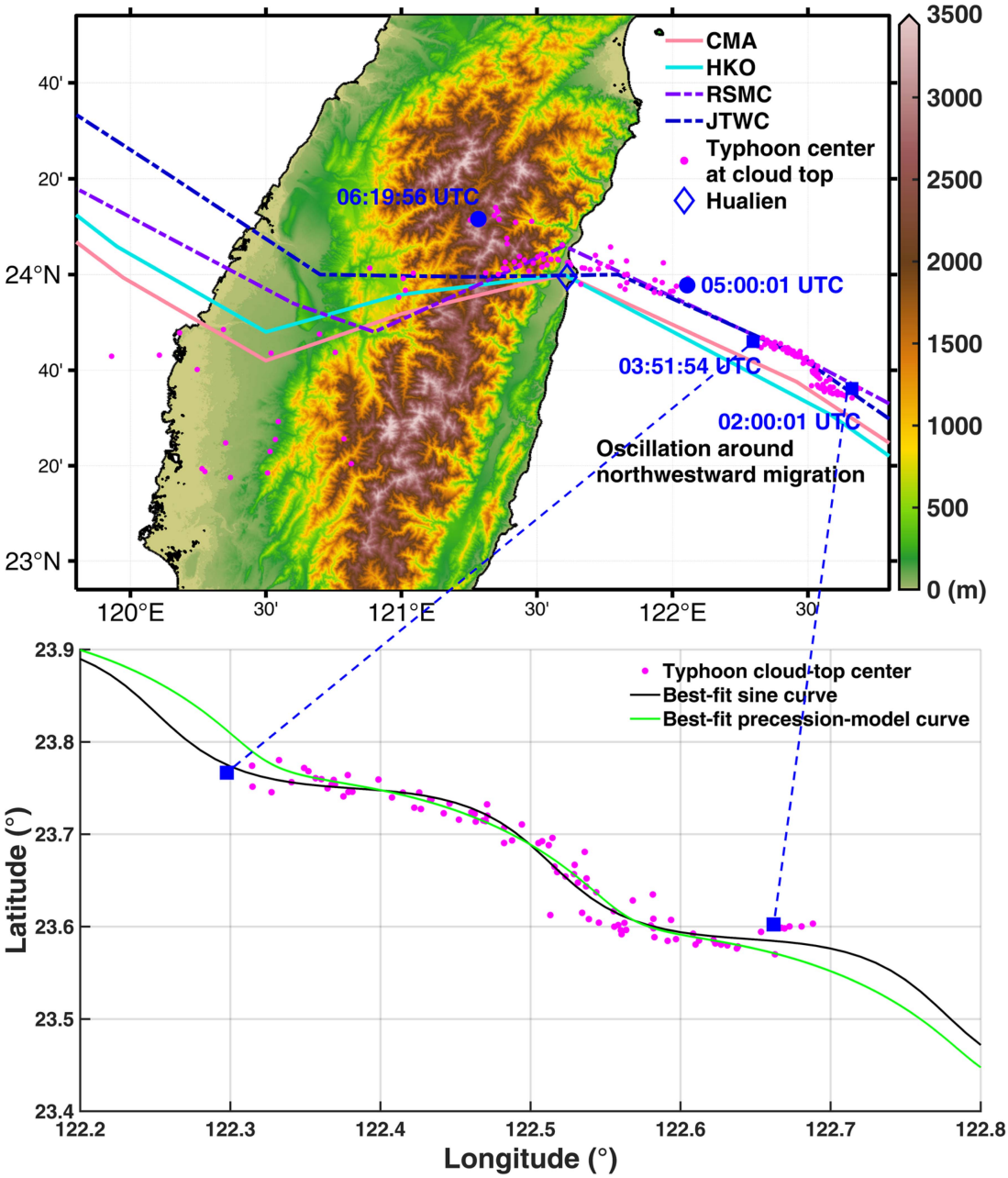

Fig. 4. Results of automatically located the cloud-top center of Typhoon Megi (2016) at 1-min intervals. In the upper panel, the magenta dots denote the located center positions, the blue solid squares mark the starting and ending center positions of the first imaging session, and the blue solid circles mark the starting and ending center positions of the period of the second imaging session before 06:20, 27 September (UTC). The located center positions gradually became scattered, and after 06:20 UTC, they were no longer consistently representative of the actual positions of Megi's cloud-top center. At the same time, the typhoon system as a whole continuously migrated in the same direction as before. The polygonal pink, cyan, violet, and blue lines link Megi's center positions in the 3-h-interval records of the BT data sets of four meteorological agencies: China Meteorological Administration (CMA), the Hong Kong Observatory (HKO), the Regional Specialized Meteorological Center (RSMC) of Japan, and the Joint Typhoon Warning Center (JTWC). The BT data sets were integrated into the international BT archive for climate stewardship (IBTrACS). The background of the upper panel is the GMTED 7.5-arc-second resolution topography map. During the first imaging session, Megi's cloud-top center presented small-scale oscillation along its general northwestward migration. The lower panel shows the sine fitting (black curve) and precession fitting (green curve) of the located center positions (magenta dots) during the first imaging session.

clusters before 06:20 UTC. The general migration of Typhoon Megi's cloud-top center is overall consistent with the BT data presented as the polygonal lines linking the typhoon center positions in the 3-h-interval BT records. In the upper panel of Fig. 5, the cloud-top average rotation and divergence speeds (see Section III-A) are plotted to indicate the rapid strength variation of the cloud-top rotation and divergence motion fields. The lower panel of Fig. 5 shows the average elevation beneath Typhoon Megi. The decrease in the cloud-top average rotation speed is consistent with the decrease in the typhoon intensity indicated

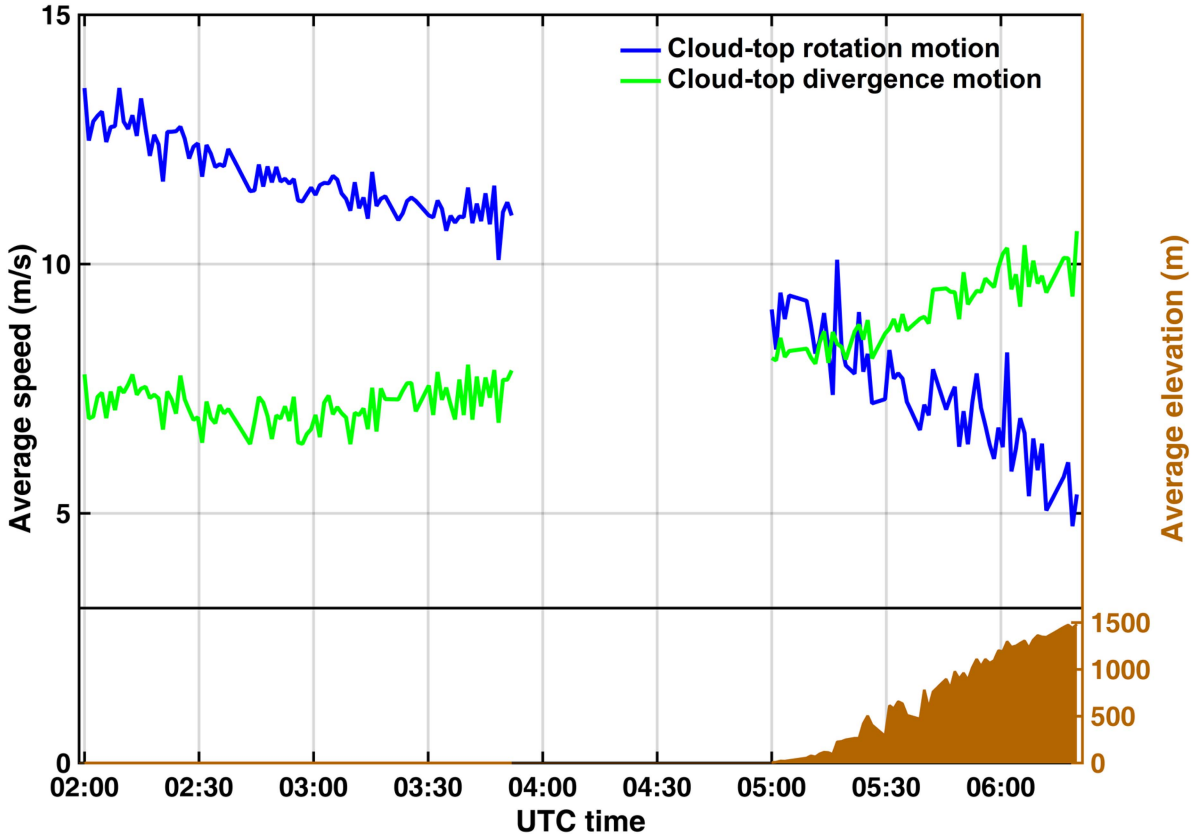

Fig. 5. Variation of the cloud-top average rotation and divergence speeds of Typhoon Megi (2016). Megi's cloud-top motion field is decomposed into the rotation, divergence, and harmonic motion fields by the Green function-based algorithm with an open boundary. Within the 150-km-radius circles centered at Megi's cloud-top center positions, we averaged the speeds (magnitudes of velocity vectors) in the cloud-top rotation and divergence motion fields, respectively. We used the so-calculated 150-km-radius average rotation and divergence speeds to indicate the strength variations of Megi's cloud-top rotation and divergence motion fields. The top part shows the average rotation and divergence speeds at 1-min intervals. The bottom part shows the variation of the 50-km-radius average elevation along the typhoon path in the ETOPO1 1-arc-minute resolution topography map. The 50-km radius can cover the ground footage of most TC eye sizes [15]. The average elevation is to give a representative relief terrain variation beneath Megi.

TABLE I
BT RECORDS OF MAXIMUM SURFACE (10-M HEIGHT ABOVE GROUND LEVEL) WIND SPEEDS AND CENTRAL PRESSURES OF TYPHOON MEGI (2016) COVERING ITS LANDFALL EVENT ON 27 SEPTEMBER 2016

UTC time	Maximum wind speed (m/s)				Center pressure (hPa)			
	CMA	HKO	RSMC	JTWC	CMA	HKO	RSMC	JTWC
00:00	52	49	44	59	940	940	945	937
03:00	48	47	44	55	945	942	945	942
06:00 (landfall)	45	46	41	51	950	945	950	948
09:00	42	42	39	46	955	952	960	955

by the maximum surface wind speed and central pressure in the BT records (see Table I). However, our results reveal more details on the cloud-top motion variation.

A. *Shift of Typhoon Megi's Cloud-Top Center*

During the first imaging session, Typhoon Megi's cloud-top center generally migrated northwestward, as shown in the upper panel of Fig. 4, but the trend was accompanied by small-scale oscillation along it. We applied the methods described in Section III-B to quantitatively characterize the kinematic property of the oscillation as shown in the lower panel of Fig. 4 where the best-fit sine model (black curve) and precession model (green curve) of Typhoon Megi's cloud-top center positions (magenta dots) are presented. According to the sine-curve fitting method, the oscillation's amplitude, spatial period, and temporal period are estimated to be ∼0.023° (∼2.4 km), ∼0.31° (∼33 km), and ∼1.46 h, respectively; while for the precession-model-curve fitting method, they are ∼0.015° (∼1.6 km), ∼0.29° (∼31 km), and ∼1.48 h. The results of the two methods are overall consistent with each other. In addition, the precession-model-curve fitting method suggests that Typhoon Megi's cloud-top center rotated anticlockwise.

The previous observation studies of wobbling TC centers indicate that the oscillation period of the phenomenon typically ranges from tens of minutes to more than 10 h, and

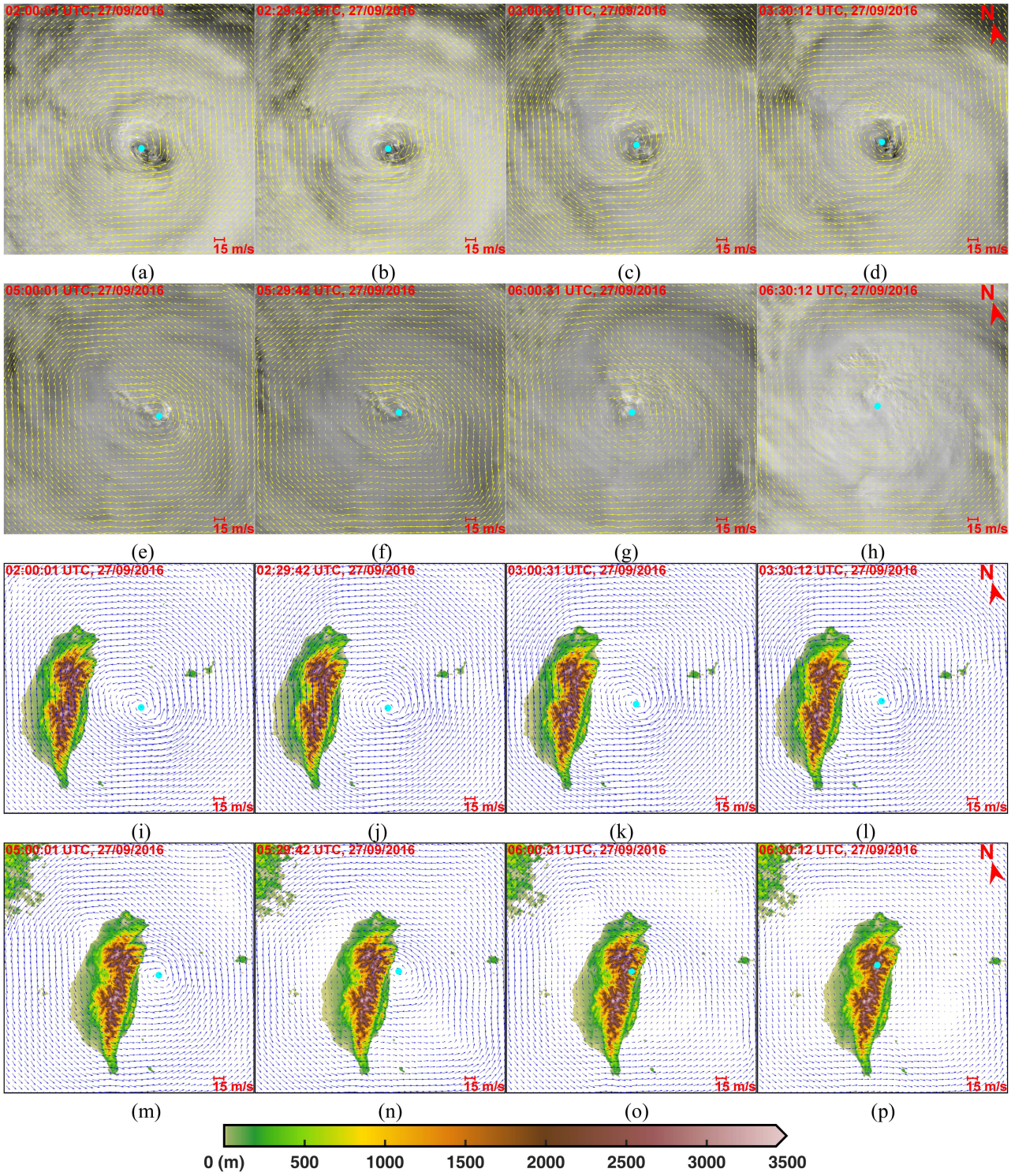

Fig. 6. Cloud-top rotation motion field of Typhoon Megi (2016) at 30-min intervals during the two imaging sessions. (a)–(h) Backgrounds are cloud images acquired by the GF-4 satellite. (i)–(p) Backgrounds are the ETOPO1 topography map. For clarity, the cloud-top rotation motion field is denoted by yellow and blue arrows in (a)–(h) and (i)–(p), respectively. The cyan dots represent Megi's cloud-top center positions. (a)–(d) and (i)–(l) Cloud-top rotation motion field during the first imaging session, whereas (e)–(h) and (m)–(p) Second imaging session. Each image covers ~512 km × 512 km.

the oscillation amplitude ranges from several kilometers to 30 km [32], [33], [34], [35], [36], [37], [38]. To our knowledge on the topic from literature, most satellite observation studies are only for the large-scale TC-center-wobbling phenomenon due to low spatial-temporal resolution. In this study, the very small-scale oscillation of Typhoon Megi's cloud-top center and the kinematic characteristics were successfully extracted from the satellite cloud images. Thus, our study provides a way to quantitatively observe details of much smaller scale oscillations of TC-cloud-top-center migration.

Based on the data in the upper panel of Fig. 4, we visually estimated the migration distances of Typhoon Megi's cloud-top center during the first imaging session and during the prelandfall period of the second imaging session, respectively, and then divided the distances by the corresponding time intervals (1.87 h and 0.86 h) to work out the relevant migration speeds (not including high-frequency motions, e.g., the small-scale oscillation), which are roughly ∼22 km/h and ∼58 km/h over the sea surface during the first and second imaging sessions, respectively. We also estimated the migration speed during the first imaging session using the sine-curve fitting and the precession-model-curve fitting, respectively. Such estimated speeds are ∼22 km/h and ∼21 km/h, confirming the visual estimation. The migration accelerated dramatically by 1.6 times in only ∼2.5 h between the first imaging session's middle and the middle of the prelandfall period of the second imaging session.

After landfall, Typhoon Megi's cloud-top center gradually deflected southward. Later, the typhoon eye disappeared at the cloud top to become a central plate with periphery clouds rotating around it [see Fig. 6(h)]. Visual observation of the top cloud features in the GF-4 images indicates that Typhoon Megi was still a cyclone as a whole but no longer a simple rotation system according to the deformation of the cloud-top rotation motion field. Because of interaction with the high-relief terrain of the Central Mountain Range, the internal motion of Typhoon Megi was rapidly changing its structures, with multiple swirls appearing and disappearing quickly in different positions within the typhoon system. They could be detected as cloud-top rotation centers, if their motions have a higher degree of curling than the visual center. As a result, the cloud-top rotation center positions detected from the cloud-top rotation motion field after 06:20 UTC are scattered (see the upper panel of Fig. 4) and no longer consistently representative of the actual positions of Typhoon Megi's cloud-top center. Meanwhile, the typhoon system as a whole continuously migrated in the direction of its previous path.

B. *Variation of Typhoon Megi's Cloud-Top Rotation and Divergence Motions*

Fig. 6(a)–(d) presents that the swirling clouds rotating around the typhoon eye form a disk during the first imaging session. The overlaid cloud-top rotation motion field was consistent with the top cloud features except for gradually deforming in the north-northwest (NNW) of Typhoon Megi's cloud-top center. Fig. 6(i)–(l) shows that the deformation mainly occurred over the Central Mountain Range. Thus, the deformation is considered the response of Typhoon Megi's cloud-top motion to the high mountain range, resulting in a gentle weakening of the cloud-top rotation motion (see Fig. 5). Meanwhile, the strength of the cloud-top divergence motion was steady before ∼03:00 UTC and then began to increase. The graph of the cloud-top average divergence speed captures the turning moment (see Fig. 5).

As shown in Fig. 6(e)–(h), Typhoon Megi maintained its swirling cloud structure with an eye in the center of the cloud top till its landfall over Hualien at ∼06:00 UTC. But soon after, Typhoon Megi's central area encountered the high-relief terrain of the Central Mountain Range and as Fig. 5 shows, the cloud-top average rotation speed decreased nearly linearly much faster than during the first imaging session. Contrarily, the cloud-top divergence motion kept on strengthening. The cloud-top average divergence speed became even higher than the cloud-top average rotation speed after ∼05:30 UTC before the typhoon landfall and further increased to ∼2 times the cloud-top average rotation speed at ∼06:20 UTC after the landfall. This result indicates that Typhoon Megi's cloud-top motion rapidly changed from a typical rotation motion-dominated status to a divergence motion-dominated status.

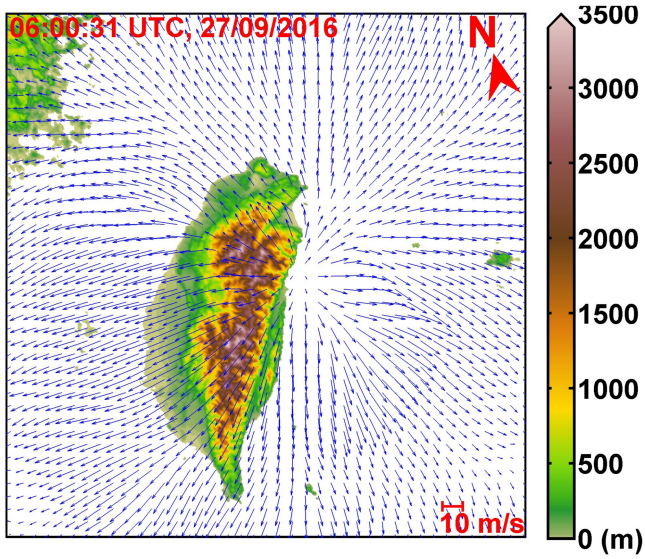

Fig. 7. Cloud-top divergence motion field of Typhoon Megi (2016) at 06:00 UTC. The image covers ∼512 km × 512 km.

The Central Mountain Range could cause the above phenomenon of a quickly weakening rotation motion accompanied by a rapid strengthening of divergence motion at the cloud top.

Weakening rotation motion: As Typhoon Megi approached Taiwan Island, the elevation beneath Typhoon Megi dramatically increased (see Fig. 5). Correspondingly, the relative vorticity quickly decreased according to the barotropic potential vorticity conservation equation [39]. Thus, the rotation motion would rapidly weaken. In addition, the Central Mountain Range blocked Typhoon Megi's energy source of latent heat from warm seawater, and its rugged terrain impeded the wind field of Typhoon Megi by friction. All these would contribute to weakening the rotation motion of Typhoon Megi.

Strengthening divergence motion: The fast reduction of the relative vorticity would be achieved by the strong divergence motion according to the vorticity equation [39]. In addition, the high mountain range was a massive blockage on Typhoon Megi's migration path, which would block the warm, moist horizontal airflows and force the airflows upward along the mountain flanks facing the wind. The upward airflows would result in divergent airflows at the cloud top. As shown in Fig. 7, the cloud-top divergence motion field presented an asymmetry pattern: the cloud-top divergence motion in the western area (the bottom-left part of Fig. 7) covering the Central Mountain Range was stronger than that in the eastern area (the top-right

TABLE II
AVERAGES OF THE ERA5 100-HPA LEVEL (ABOUT 16 KM ALTITUDE) VERTICAL VELOCITY DATA OF AIR MOTION WITHIN THE 150-KM-RADIUS CIRCLES CENTERED AT THE CLOUD-TOP CENTER POSITIONS OF TYPHOON MEGI ON 27 SEPTEMBER 2016

UTC time	02:00	03:00	05:00	06:00
Average vertical velocity (Pa/s)	−0.0453	−0.0497	−0.0532	−0.0919

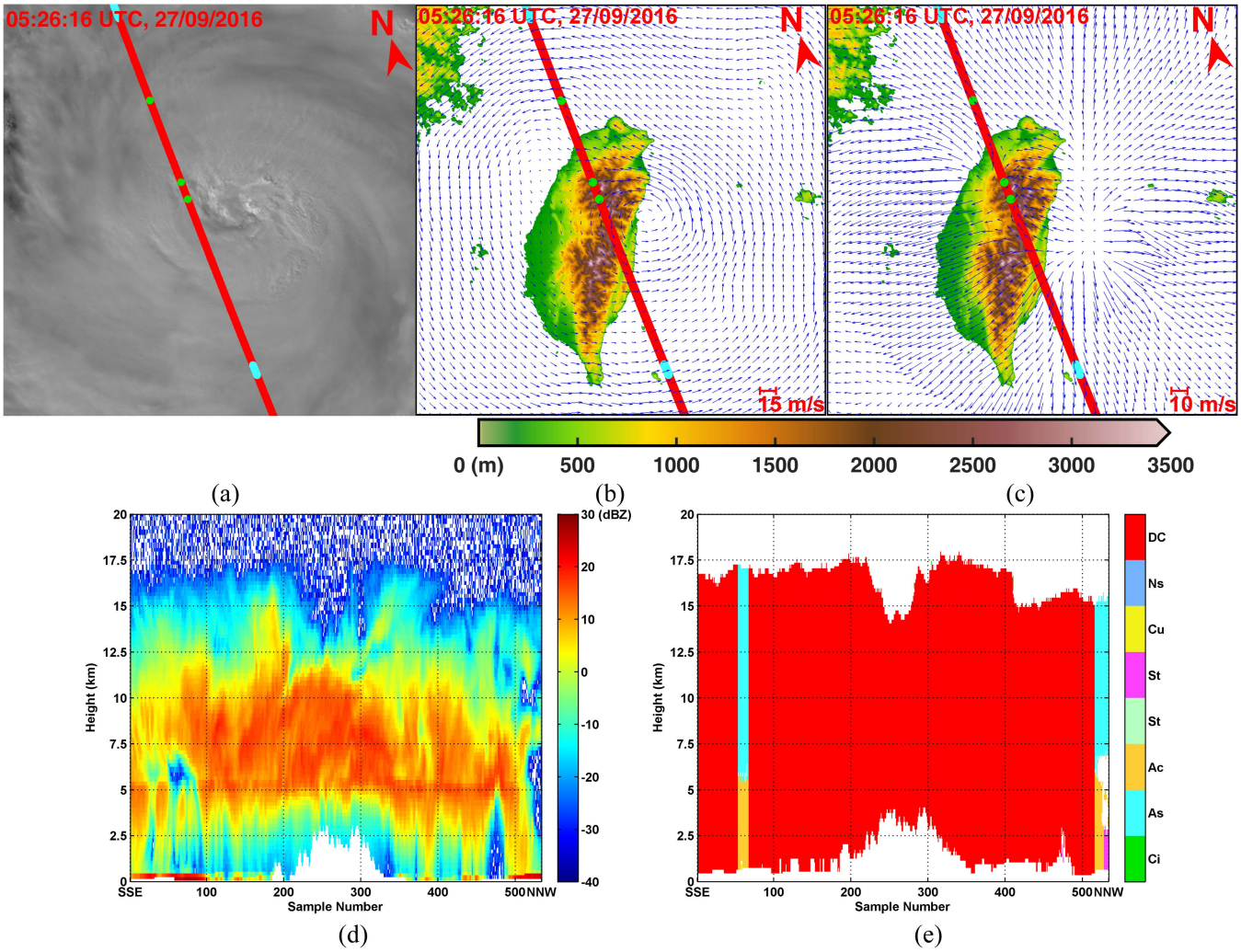

Fig. 8. Track, radar reflectivity measurement, and cloud classification of the Cloudsat satellite. The Cloudsat satellite overpassed the west of the central area of Typhoon Megi (2016) at 05:26, 27 September (UTC). The satellite track is drawn on (a) GF-4 cloud image, (b) cloud-top rotation motion field overlaying the ETOPO1 topography map, and (c) cloud-top divergence motion field overlaying the ETOPO1 topography map. (a)–(c) Cover ∼512 km × 512 km. The colors in the track in (a)–(c) denote the cloud types at the cloud top. (d) and (e) present the vertical distributions of radar reflectivity and cloud type along the satellite track shown in (a)–(c). The labels "SSE" and "NNW" on the horizontal axis in (d) and (e) correspond to the south-southeast to north-northwest (SSE-NNW) direction of the track in (a)–(c). Clouds are classified into eight types that is cirrus (Ci), altostratus (As), altocumulus (Ac), stratus (St), stratocumulus (Sc), cumulus (Cu), nimbostratus (Ns), and deep convective (DC).

part of Fig. 7). Moreover, when a TC migrates faster than the surrounding lower-level airflows, the speed difference can induce net air inflows to strengthen the convergent upward motion at the lower level ahead of the TC [40]. Considering the airflow continuity, the air outflows will strengthen at the upper level. Thus, the dramatic increase in Typhoon Megi's migration speed before landfall (see Paragraph 3 in Section IV-A) could also contribute to strengthening the cloud-top divergence motion.

The ERA5 data has a temporal resolution of 1 h. Table II presents the averages of the ERA5 100-hPa level (about 16-km altitude) vertical velocity data of air motion at 02:00, 03:00, 05:00, and 06:00 UTC corresponding to GF-4's two imaging sessions, within the 150-km-radius circles centered at the cloud-top center positions of Typhoon Megi. It indicates that the upward air motion in Typhoon Megi's central area notably increased after 03:00 UTC when the cloud-top divergence motion dramatically enhanced.

Fig. 8(d) and (e) presents the vertical distributions of radar reflectivity and cloud type along the track of the CloudSat satellite shown in Fig. 8(a)–(c). Fig. 8(e) illustrates that the clouds distributed in the vertical section are almost all thick deep

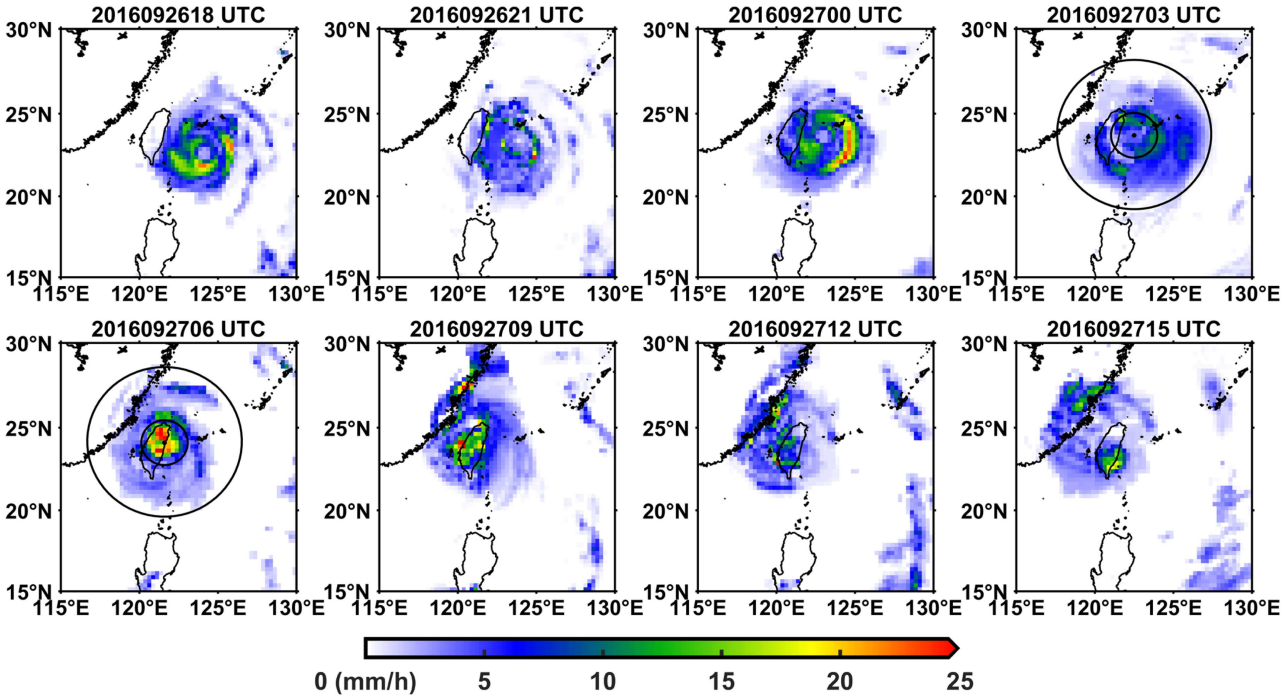

Fig. 9. TMPA data show a dramatic precipitation increase over mountainous Taiwan Island during the landfall of Typhoon Megi (2016). The precipitation over Taiwan Island was weaker at 03:00 UTC than at other times. It dramatically increased to ∼25 mm/h at 06:00 UTC (the landfall time). The black circles are 150 km and 500 km in radius, centered at Megi's center positions at 03:00 UTC and 06:00 UTC. We averaged the TMPA precipitation data within the 150-km-radius circle and the ring (area between the 150-km inner circle and 500-km outer circle). The 150-km-radius circle precipitation averages are 7.22 mm/h and 12.74 mm/h at the two times, respectively, showing an increase of 5.52 mm/h. The ring area precipitation averages are 2.63 mm/h and 1.68 mm/h, showing a decrease of 0.95 mm/h. Thus, the precipitation-increasing area was mainly distributed within Megi's central area.

convective clouds. The top of the deep convective clouds was as high as 17.5 km near Typhoon Megi's central area. Plentiful deep convective clouds usually suggest strong deep convections that generate air outflows at the upper level [26]. Thus, the strengthening cloud-top divergence motion revealed in our results is consistent with the thick deep convective clouds revealed by the CloudSat satellite. Furthermore, the strong radar reflection in Fig. 8(d) indicates that the deep convective clouds contained a large amount of liquid and ice water that would produce heavy precipitation during landfall, although the landfall time is in the weak-precipitation phase of typhoon precipitation diurnal variation [41].

Fig. 9 presents the TMPA precipitation data that cover the typhoon landfall event. The precipitation over mountainous Taiwan Island was weaker at 03:00 UTC than at the other times. Then, it dramatically increased to ∼25 mm/h at 06:00 UTC (the landfall time) in areas mainly distributed within a 150-km radius from the typhoon center. In addition, the daily precipitations in many areas on Taiwan Island suddenly increased to >200 mm and even reached 327 mm in the Alishan area on 27 September 2016 (local time, UTC+8 h). As shown in Fig. 9, such severe rainstorms occurred mainly during landfall. The rapid precipitation increase is consistent with the dramatic strengthening of the cloud-top divergence motion in the time as indicated by the graph of 150-km-radius average divergence speed in Fig. 5. Obviously, high-frequency observation of a typhoon system's cloud-top divergence motion field could provide vital information on the rapid variation of the relating precipitation intensity.

V. Summary

The GF-4 satellite acquired 50-m-1-min-resolution successive cloud images of Typhoon Megi (2016) landfall over mountainous Taiwan Island. We developed an automatic analysis methodology, which enables the extraction of detailed information of TC systems from high spatial-temporal resolution cloud images. It derived Typhoon Megi's cloud-top rotation and divergence motion fields from the GF-4 images, located Typhoon Megi's cloud-top center positions at 1-min intervals from the rotation motion field, calculated Typhoon Megi's cloud-top average rotation and divergence speeds, and extracted the migration oscillation kinematic characteristics of Typhoon Megi's cloud-top center.

Two methods, as part of our methodology, are proposed in this article to extract the migration oscillation kinematic characteristics. The amplitude, spatial period, and temporal period of the oscillation are estimated to be ∼2.4 km, ∼33 km, and ∼1.46 h by the sine-curve-fitting method, while ∼1.6 km, ∼31 km, and ∼1.48 h by the precession-model-curve fitting method. In addition, the precession-model-curve fitting method suggests that Typhoon Megi's cloud-top center rotated anticlockwise.

Approaching landfall, the migration speed of Typhoon Megi's cloud-top center dramatically accelerated by ∼1.6 times (from ∼22 to ∼58 km/h) in only ∼2.5 h. After landfall, the cloud-top center migration deflected southward from its general northwest direction before landfall. Meanwhile, the located center positions gradually became scattered.

Typhoon Megi's cloud-top rotation motion quickly weakened during the landfall event, whereas the cloud-top divergence motion rapidly strengthened from its initially steady status. The cloud-top average divergence speed increased by ∼30% in only ∼2.5 h, reaching up to ∼2 times the average rotation speed. The cloud-top average divergence speed graph captures the turning moment. The result reveals that Typhoon Megi's cloud-top motion rapidly transformed from typical rotation motion dominance to divergence motion dominance. The extreme cloud-top divergence motion is highly related to intense upward warm and moist airflows that usually cause sudden heavy precipitation.

Thus, our study explores a satellite-observation way to mine the information on the high-frequency variation of typhoon cloud-top motion. The information may help monitor TCs' rapid change in remote areas without in-site observations.

ACKNOWLEDGMENT

The GF-4 first-band (panchromatic band, 0.45–0.90 μm) images are from the China Centre for Resources Satellite Data and Application (can be accessed by the search box on https://data.cresda.cn/#/2dMap). The IBTrACS version 4 and the ETOPO1 topography map are from the NOAA NCEI (https://www.ncei.noaa.gov/products/international-best-track-archive and https://www.ncei.noaa.gov/products/etopo-global-relief-model). The GMTED topography map is from the USGS EROS Center (https://www.usgs.gov/centers/eros/science/usgs-eros-archive-digital-elevation-global-multi-resolution-terrain-elevation?qt-science_center_objects = 0#qt-science_center_objects). The CloudSat 2B-GEOPROF and 2B-CLDCLASS products including the radar reflectivity and cloud type data are from JPL (https://cloudsat.atmos.colostate.edu/data). The TRMM TMPA 3B42 version-7 products are from the NASA EOSDIS (https://disc.gsfc.nasa.gov/datasets/TRMM_3B42_Daily_7/summary). The ERA5 data are from the ECMWF (https://cds.climate.copernicus.eu/cdsapp#!/dataset/reanalysis-era5-pressure-levels?tab = overview).

REFERENCES

[1] T. R. Knutson, J. L. McBride, and J. Chan, "Tropical cyclones and climate change," *Nature Geosci.*, vol. 3, pp. 157–163, Mar. 2010, doi: 10.1038/ngeo779.

[2] M. A. Bender, T. R. Knutson, and R. E. Tuleya, "Modeled impact of anthropogenic warming on the frequency of intense Atlantic hurricanes," *Science*, vol. 327, pp. 454–458, Jan. 2010, doi: 10.1126/science.1180568.

[3] J. B. Elsner, J. P. Kossin, and T. H. Jagger, "The increasing intensity of the strongest tropical cyclones," *Nature*, vol. 455, no. 4, pp. 92–95, Sep. 2008, doi: 10.1038/nature07234.

[4] K. Emanuel, "Increasing destructiveness of tropical cyclones over the past 30 years," *Nature*, vol. 436, pp. 686–688, Aug. 2005, doi: 10.1038/nature03906.

[5] R. Mendelsohn et al., "The impact of climate change on global tropical cyclone damage," *Nature Climate Change*, vol. 2, pp. 205–209, Mar. 2012, doi: 10.1038/nclimate1357.

[6] P. Peduzzi, B. Chatenoux, and H. Dao, "Global trends in tropical cyclone risk," *Nature Climate Change*, vol. 2, no. 4, pp. 289–294, Apr. 2012, doi: 10.1038/nclimate1410.

[7] M.-D. Leroux et al., "Recent advances in research and forecasting of tropical cyclone track, intensity, and structure at landfall," *Trop. Cyclone Res. Rev.*, vol. 7, no. 2, pp. 85–105, May 2018, doi: 10.6057/2018TCRR02.02.

[8] S. Guan, S. Li, Y. Hou, P. Hu, Z. Liu, and J. Feng, "Increasing threat of landfalling typhoons in the western North Pacific between 1974 and 2013," *Int. J. Appl. Earth Observ. Geoinf.*, vol. 68, pp. 279–286, Jun. 2018, doi: 10.1016/j.jag.2017.12.017.

[9] I.-J. Moon, S.-H. Kim, and J. C. L. Chan, "Climate change and tropical cyclone trend," *Nature*, vol. 570, pp. E3–E5, Jun. 2019, doi: 10.1038/s41586-019-1222-3.

[10] Q. Wang et al., "Tropical cyclones act to intensify El Niño," *Nature Commun.*, vol. 10, Aug. 2019, Art. no. 3793, doi: 10.1038/s41467-019-11720-w.

[11] X. Yang, X. Li, Q. Zheng, X. Gu, W. G. Pichel, and Z. Li, "Comparison of ocean-surface winds retrieved from QuikSCAT scatterometer and Radarsat-1 SAR in offshore waters of the US west coast," *IEEE Geosci. Remote Sens. Lett.*, vol. 8, no. 1, pp. 163–167, Jan. 2011, doi: 10.1109/LGRS.2010.2053345.

[12] H. Wang, J. Zhu, M. Lin, Y. Zhang, and Y. Chang, "Evaluating Chinese HY-2B HSCAT ocean wind products using buoys and other scatterometers," *IEEE Geosci. Remote Sens. Lett.*, vol. 17, no. 6, pp. 923–927, Jun. 2020, doi: 10.1109/LGRS.2019.2940384.

[13] J. Zou, Z. Wang, and M. Lin, "Analysis of the high-latitude sea surface wind acquisition ability of seven satellite scatterometers," *IEEE Geosci. Remote Sens. Lett.*, vol. 19, 2022, Art. no. 1501805, doi: 10.1109/LGRS.2020.3046601.

[14] X. Yin, Z. Wang, Q. Song, Y. Huang, and R. Zhang, "Estimate of ocean wind vectors inside tropical cyclones from polarimetric radiometer," *IEEE Sel. Topics Appl. Earth Observ. Remote Sens.*, vol. 10, no. 5, pp. 1701–1714, May 2017, doi: 10.1109/JSTARS.2017.2667040.

[15] X. Li et al., "Tropical cyclone morphology from spaceborne synthetic aperture radar," *Bull. Amer. Meteorol. Soc.*, vol. 94, no. 2, pp. 215–230, Feb. 2013, doi: 10.1175/BAMS-D-11-00211.1.

[16] A. K. Liu, Y. H. Cheng, C. R. Ho, S.-J. Huang, and N.-J. Kuo, "Typhoon eye observations using SAR and MTSAT," in *Typhoon Impact and Crisis Management Advances in Natural and Technological Hazards Research*, vol. 40, D. Tang and G. Sui Eds., Berlin, Germany: Springer-Verlag, 2014, pp. 63–79, doi: 10.1007/978-3-642-40695-9_3.

[17] G. Zheng, J. Yang, A. K. Liu, X. Li, W. Pichel, and S. He, "Comparison of typhoon centers from SAR and IR images and those from best track data sets," *IEEE Trans. Geosci. Remote Sens.*, vol. 54, no. 2, pp. 1000–1012, Feb. 2016, doi: 10.1109/TGRS.2015.2472282.

[18] G. Zhang, W. Perrie, X. Li, and J. A. Zhang, "A hurricane morphology and sea surface wind vector estimation model based on C-band cross-polarization SAR imagery," *IEEE Trans. Geosci. Remote Sens.*, vol. 55, no. 3, pp. 5244–5260, Mar. 2017, doi: 10.1109/TGRS.2016.2631663.

[19] G. Zheng et al., "Development of a gray-level co-occurrence matrix-based texture orientation estimation method and its application in sea surface wind direction retrieval from SAR imagery," *IEEE Trans. Geosci. Remote Sens.*, vol. 56, no. 9, pp. 5244–5260, Sep. 2018, doi: 10.1109/TGRS.2018.2812778.

[20] Y. Wang et al., "An automatic algorithm for estimating tropical cyclone centers in synthetic aperture radar imagery," *IEEE Trans. Geosci. Remote Sens.*, vol. 60, 2022, Art. no. 4203716, doi: 10.1109/TGRS.2021.3105705.

[21] L. Zhou et al., "Sea surface wind speed retrieval from textures in synthetic aperture radar imagery," *IEEE Trans. Geosci. Remote Sens.*, vol. 60, 2022, Art. no. 4200911, doi: 10.1109/TGRS.2021.3062401.

[22] F. Sun, M. Min, D. Qin, F. Wang, and J. Hu, "Refined typhoon geometric center derived from a high spatiotemporal resolution geostationary satellite imaging system," *IEEE Geosci. Remote Sens. Lett.*, vol. 16, no. 4, pp. 499–503, Apr. 2019, doi: 10.1109/LGRS.2018.2876895.

[23] J. Liu, G. Zheng, J. Yang, and J. Wang, "Top cloud motion field of Typhoon Megi-2016 revealed by GF-4 images," *IEEE Trans. Geosci. Remote Sens.*, vol. 57, no. 7, pp. 4427–4444, Jul. 2019, doi: 10.1109/TGRS.2019.2891207.

[24] G. Zheng, J. Liu, J. Yang, and X. Li, "Automatically locate tropical cyclone centers using top cloud motion data derived from geostationary satellite images," *IEEE Trans. Geosci. Remote Sens.*, vol. 57, no. 12, pp. 10175–10190, Dec. 2019, doi: 10.1109/TGRS.2019.2931795.

[25] R. Marchand, G. G. Mace, T. Acherman, and G. Stephens, "Hydrometeor detection using Cloudsat—An earth-orbiting 94-GHz cloud radar," *J. Atmos. Ocean. Technol.*, vol. 25, no. 4, pp. 519–533, Apr. 2008, doi: 10.1175/2007JTECHA1006.1.

[26] K. Sassen and Z. Wang, "Classifying clouds around the globe with the CloudSat radar: 1-year of results," *Geophys. Res. Lett.*, vol. 35, no. 4, Feb. 2008, Art. no. L04805, doi: 10.1029/2007GL032591.

[27] K. V. Subrahmanyam, K. K. Kumar, and N. D. Tourville, "CloudSat observations of three-dimensional distribution of cloud types in tropical cyclones," *IEEE Sel. Topics Appl. Earth Observ. Remote Sens.*, vol. 11, no. 2, pp. 339–344, Feb. 2018, doi: 10.1109/JSTARS.2017.2786666.
[28] G. J. Huffman et al., "The TRMM multisatellite precipitation analysis (TMPA): Quasi-global, multiyear, combined-sensor precipitation estimates at fine scales," *J. Hydrometeorology*, vol. 8, no. 1, pp. 38–55, Feb. 2007, doi: 10.1175/JHM560.1.
[29] G. L. K. Morgan, J. G. Liu, and H. Yan, "Precise subpixel disparity measurement from very narrow baseline stereo," *IEEE Trans. Geosci. Remote Sens.*, vol. 48, no. 9, pp. 3424–3433, Sep. 2010, doi: 10.1109/TGRS.2010.2046672.
[30] J. Liu, H. Yan, and G. Morgan, "PCIAS subpixel technology," *Meas. Control*, vol. 45, no. 7, pp. 207–211, Sep. 2012, doi: 10.1177/002029401204500702.
[31] X. Wan, J. Liu, H. Yan, and G. L. Morgan, "Illumination-invariant image matching for autonomous UAV localization based on optical sensing," *ISPRS J. Photogrammetry Remote Sens.*, vol. 119, pp. 198–213, Sep. 2016, doi: 10.1016/j.isprsjprs.2016.05.016.
[32] M. B. Lawrence and B. M. Mayfield, "Satellite observations of trochoidal motion during hurricane Belle 1976," *Monthly Weather Rev.*, vol. 105, no. 11, pp. 1458–1461, Nov. 1977, doi: 10.1175/1520-0493(1977)105%3C1458:SOOTMD%3E2.0.CO;2.
[33] T. Muramatsu, "Trochoidal motion of the eye of Typhoon 8019∗," *J. Meteorological Soc. Jpn.*, vol. 64, no. 2, pp. 259–272, Apr. 1986, doi: 10.2151/jmsj1965.64.2_259.
[34] J. S. Griffin et al., "Real-time airborne analysis of aircraft data supporting operational hurricane forecasting," *Weather Forecasting*, vol. 7, no. 3, pp. 480–490, Sep. 1992, doi: 10.1175/1520-0434(1992)007<0480:RTAAOA>2.0.CO;2.
[35] F. Roux and N. Viltard, "Structure and evolution of hurricane Claudette on 7 September 1991 from airborne Doppler radar observations. Part I: Kinematics," *Monthly Weather Rev.*, vol. 123, no. 9, pp. 2611–2639, Sep. 1995, doi: 10.1175/1520-0493(1995)123%3C2611:SAEOHC%3E2.0.CO;2.
[36] J.-S. Hong and P.-L. Chang, "The trochoid-like track in Typhoon Dujuan (2003)," *Geophys. Res. Lett.*, vol. 32, no. 16, Aug. 2005, Art. no. L16801, doi: 10.1029/2005GL023387.
[37] F. D. Marks et al., "Structure of the eye and eyewall of Hurricane Hugo (1989)," *Monthly Weather Rev.*, vol. 136, no. 4, pp. 1237–1259, Apr. 2008, doi: 10.1175/2007MWR2073.1.
[38] Y. Feng and L. Wu, "Small-amplitude trochoidal oscillations in Typhoons Rammasun (2014) and Lekima (2019)," *Terr., Atmos. Ocean. Sci.*, vol. 32, no. 6, pp. 1153–1162, Dec. 2021, doi: 10.3319/TAO.2021.07.26.02.
[39] J. R. Holton and G. J. Hakim, *An Introduction to Dynamic Meteorology*, 5th ed. Amsterdam, The Netherlands: Elsevier, 2013, pp. 95–125, doi: 10.1016/B978-0-12-384866-6.00004-0.
[40] S. Tu, J. C. L. Chan, J. Xu, Q. Zhong, W. Zhou, and Y. Zhang, "Increase in tropical cyclone rain rate with translation speed," *Nature Commun.*, vol. 13, Nov. 2022, Art. no. 7325, doi: 10.1038/s41467-022-35113-8.
[41] Q. Wu, Z. Ruan, D. Chen, and T. Liao, "Diurnal variations of tropical cyclone precipitation in the inner and outer rainbands," *J. Geophysical Res., Atmos.*, vol. 120, no. 1, pp. 1–11, Jan. 2015, doi: 10.1002/2014JD022190.

Gang Zheng (Senior Member, IEEE) received the B.Eng. degree in electronic information engineering from Zhejiang University, Hangzhou, China, in 2003, and the M.S. and Ph.D. degrees in radio physics from the University of Electronic Science and Technology of China, Chengdu, China, in 2006 and 2010, respectively.

From 2010 to 2013, he was an Assistant Researcher with the State Key Laboratory of Satellite Ocean Environment Dynamics, Second Institute of Oceanography, Ministry of Natural Resources, Hangzhou, China, where he was an Associate Researcher, from 2013 to 2020, and has been a Researcher, since 2020. He also has been an Adjunct Researcher with the Ocean College, Zhejiang University, and an Adjunct Professor with the College of Oceanography, Hohai University, Nanjing, China, since 2022. His current research interests include ocean microwave remote sensing, artificial intelligence applications, image processing, and electromagnetic numerical modeling.

Dr. Zheng serves as an Associate Editor of Remote Sensing in Ecology and Conservation, an Editorial Board Member of the Ocean Section of Remote Sensing, and a Topic Editor of Big Earth Data.

Jianguo Liu (Senior Member, IEEE) received the M.Sc. degree in remote sensing for geology from China University of Geosciences, Beijing, China, in 1982, and the Ph.D. degree in remote sensing and image processing from Imperial College London, U.K., in 1991.

He was a Reader in Remote Sensing till 2019 with the Department of Earth Science and Engineering, Imperial College London, and is currently an Emeritus Reader in remote sensing to carry on research in the same department after retirement. He is the principal author of two books on image processing and GIS for remote sensing and authored or coauthored more than 130 research articles. His current research interests include subpixel technology for precise image registration and feature matching, 3-D and motion data generation, illumination invariant change detection, vision-based UAV navigation and super resolution reconstruction; image processing techniques for data fusion, filtering and InSAR; and GIS multidata modeling for geohazard studies.

Liang Wu received the B.S. and Ph.D. degrees in meteorology from Sun Yat-sen University, Guangzhou, China, in 2004 and 2010, respectively.

From 2010 to 2012, he was an Assistant Professor with the Institute of Atmospheric Physics, Chinese Academy of Sciences (CAS), Beijing, China, where he was an Associate Professor, from 2013 to 2019, and has been a Professor, since 2020. He is mainly engaged in the study of tropical cyclone (TC) climatology, tropical waves and tropical atmospheric dynamics, and TCs and climate change. He has been selected as the excellent member of the Youth Innovation Promotion Association CAS. He is the Deputy Director of the Center for Monsoon System Research, Institute of Atmospheric Physics, CAS, the member of Youth Group of China National Committee for the International Association of Meteorology and Atmospheric Sciences (IAMAS), an Associate Editor of Journal, *Terrestrial, Atmospheric and Oceanic Sciences*, an Youth Editor of Journal, *The Innovation*, and an Editor of Journal, *The Innovation Geoscience*.

Peng Chen received the B.Eng. degree in photogrammetry and remote sensing from Wuhan University, Wuhan, China, in 2000, and the M.S. degree in physical oceanography from the Second Institute of Oceanography, Ministry of Natural Resources, in 2004, and the Ph.D. degree in geographic information system from the Zhejiang University, Hangzhou, China, in 2011.

From 2004 to 2009, he was an Assistant Researcher with the State Key Laboratory of Satellite Ocean Environment Dynamics, Second Institute of Oceanography, Ministry of Natural Resources, Hangzhou, China, where he was an Associate Researcher, from 2009 to 2020, and has been a Senior Engineer, since 2020. He is currently a Professor-level Senior Engineer and Postgraduate Adviser in marine remote sensing with the state key laboratory of satellite ocean environment dynamics, Hangzhou, China, working on the development of algorithms detecting marine targets, and dynamic environments.

Qiaoyan Wu received the Bachelor of Science degree in atmospheric science from Nanjing University, Nanjing, China, in 2001, the master's and Ph.D. degrees in atmospheric science from Texas A&M University, College Station, TX, USA, in 2004 and 2007, respectively.

In 2008, she joined the State Key Laboratory of Satellite Ocean Environment Dynamics, the Second Institute of Oceanography as an Associate Researcher, and was later promoted to Researcher, in 2013. Since 2018, she has been serving as an Adjunct Researcher with the Ocean School at Shanghai Jiao Tong University. Her research primarily focuses on tropical air-sea interaction, encompassing areas such as tropical cyclone air-sea interaction, monsoon variability, and ENSO variability.

Dr. Wu has been serving as an Editorial Board Member of Ocean-Land-Atmosphere Research, since 2022.

Jie Ming received the B.S. degree in atmospheric sciences and the Ph.D. degree in meteorology from Nanjing University, Nanjing, China, in 2003 and 2008, respectively.

He had about 2-year research experience with the Miami University of USA during 2007–2009, as a Visiting Scholar. From 2009–2015, he was a Lecturer with the School of Atmospheric Science, Nanjing University, Nanjing, China. Since 2016, he has been an Associate Professor with the School of Atmospheric Sciences, Nanjing University, Nanjing, China. His current research interests include typhoon numerical simulation, data assimilation and mesoscale meteorological research, focusing on the physical mechanism of the rapid intensification, and the fine structure of the typhoon.

Lizhang Zhou (Member, IEEE) received the B.S. degree in physics from Nanjing University, Nanjing, China, in 2015, and the M.S. degree in physical oceanography from the Second Institute of Oceanography, Ministry of Natural Resources, Hangzhou, China, in 2018, and the Ph.D. degree in ocean technology from the Zhejiang University, Hangzhou, China, in 2022.

He is currently an Assistant Researcher with the State Key Laboratory of Satellite Ocean Environment Dynamics, Second Institute of Oceanography, Ministry of Natural Resources, Hangzhou, China. His research interests include ocean microwave remote sensing, image processing, and artificial intelligence applications.